



ALMA MATER STUDIORUM  
UNIVERSITÀ DI BOLOGNA

## ARCHIVIO ISTITUZIONALE DELLA RICERCA

### Alma Mater Studiorum Università di Bologna Archivio istituzionale della ricerca

From HVSR to site SH response function: Potentiality and pitfalls inferred by 1D physical modelling

This is the final peer-reviewed author's accepted manuscript (postprint) of the following publication:

*Published Version:*

Paolucci E., Tanzini A., Albarello D. (2023). From HVSR to site SH response function: Potentiality and pitfalls inferred by 1D physical modelling. SOIL DYNAMICS AND EARTHQUAKE ENGINEERING, 165, 1-12 [10.1016/j.soildyn.2022.107703].

*Availability:*

This version is available at: <https://hdl.handle.net/11585/950494> since: 2023-12-12

*Published:*

DOI: <http://doi.org/10.1016/j.soildyn.2022.107703>

*Terms of use:*


Some rights reserved. The terms and conditions for the reuse of this version of the manuscript are specified in the publishing policy. For all terms of use and more information see the publisher's website.

This item was downloaded from IRIS Università di Bologna (<https://cris.unibo.it/>).  
When citing, please refer to the published version.

(Article begins on next page)

# From HVSR to site SH response function: Potentiality and pitfalls inferred by 1D physical modelling

Q5

 The corrections made in this section will be reviewed and approved by a journal production editor.

Q2

Enrico Paolucci<sup>a,\*</sup>, [enicopaolucci83@gmail.com](mailto:enicopaolucci83@gmail.com), Anna Tanzini<sup>a</sup>, Dario Albarello<sup>a,b</sup>

<sup>a</sup>Dipartimento di Scienze Fisiche, della Terra e dell'Ambiente, University of Siena, Siena, Italy

Q3

<sup>b</sup>Consiglio Nazionale delle Ricerche, Istituto di Geologia Ambientale e Geoingegneria, Rome, Italy

\*Corresponding author.

---

## Abstract

The capability of the ambient vibration Horizontal to Vertical Spectral Ratios (HVSR) in identifying the main aspects characterizing the conventional 1D site response curve was explored by physical modelling. This approach avoids possible biases induced by data processing by focusing on the underlying physical phenomenon. Moreover, differently from empirical approaches, this also allows exploring an unlimited range of subsoil configurations. By considering a huge set of realistic Vs profiles, HVSR curves were simulated and compared with the corresponding SH acceleration transfer functions (ATFs) obtained by linear equivalent numerical modelling, which is a standard for the professional practice. These comparisons focused on the values of  $F_0$  (the lowest resonance frequency),  $F_d$  (the frequency associated with maximum peak amplitude) and corresponding amplitudes ( $A_0$  and  $A_d$  respectively). Outcomes indicate that when  $F_0$  and  $F_d$  values coincide, frequency of the HVSR peak represents a reliable proxy to identify 1D resonance frequency. HVSR remains a good proxy for  $F_0$  in the remaining cases, while it is less effective concerning  $F_d$  in particular when this value is different from  $F_0$  and is identified in the frequency range 10–30 Hz. Finally, the results concerning peak amplitude values show a tendency by HVSR to underestimate in a similar way both  $A_0$  and  $A_d$  values.

---

## Keywords:

Site amplification, HVSR, SH acceleration Transfer function, Numerical modelling, Peak frequencies, Peak amplitudes

## Abbreviations

No keyword abbreviations are available

## Data availability

Data will be made available on request.

## 1 Introduction

Site seismic hazard assessment is a basic element for planning actions devoted to effectively reduce risk associated to future earthquake. Beyond large scale phenomena (activation of seismic sources, long range propagation effects), seismic hazard is largely affected by small scale seismo-stratigraphical and morphological configurations (the 'site response') responsible for ground motion amplification phenomena in the frequency range of engineering interest (e.g., Ref. [1]). In particular, interference of seismic waves trapped between main seismic impedance contrasts in the subsoil (seismic resonance phenomena) are mainly responsible for these effects, which are frequency dependent.

More or less refined, physical modelling is the main tool for assessing these effects in the lack of earthquake data and numerical codes are available on purpose and largely used in professional activity (e.g., SITE\_AMP by Boore [2]; STRATA by Kottke and Rathje [3]; SHAKE2000 by Ordóñez [4]). Feeding these models essentially requires the definition of shear wave velocity ( $V_s$ ) profile in the shallow subsoil ( $< 100\text{--}200$  m of depth) and the assessment of non-linear properties of relevant materials (shear modulus decay and damping curves). This information can be retrieved by borehole measurements and laboratory tests, whose relatively high costs can be considered as affordable when the design of single manufacts are of concern. However, when larger scale studies are considered, which is the case of seismic microzonation studies (e.g., Refs. [5–7]), simplified procedures become mandatory to make feasible the estimate of site effects at the scale of a municipality, mainly when detailed information about subsoil seismostratigraphical configuration is lacking. In these situations, fast and low-cost methods able to capture main aspects of seismic resonance phenomena come into the play. Horizontal to Vertical Spectral Ratios (HVSR) of ambient vibrations (e.g., Refs. [8–10]) have been largely used on purpose (e.g., Refs. [11–15]). Both empirical evidence and physical modelling suggest that resonance phenomena for horizontally polarized S-waves (SH) occur at the frequencies where the HVSR between average Fourier spectral amplitude of horizontal components of ambient vibrations and the respective one of vertical component reach a maximum (e.g., Refs. [16–20]). Since its relationship with the seismic impedance contrasts, this correspondence is typically used to constrain the local  $V_s$  profile by jointly inverting the HVSR curve and outcomes other active and passive array measurements (e.g., Refs. [21,22]).

However, HVSR could be also considered to directly detect and characterize seismic resonance phenomena relative to S-waves during earthquakes. In particular, this application is usually focused on the possibility of using the relative maxima of this curve to detect the dominant resonance frequency  $F_d$  characterized by the maximum amplification effect ( $A_d$  hereafter) and lowest resonance frequency  $F_0$  where some amplification  $A_0$  occurs. The importance of the resonance frequency values in delineating site response was highlighted by several investigations and site classification schemes (e.g., Refs. [23–28]) proposing these parameters ( $F_d$  or  $F_0$ ) as alternative or complementary site amplification proxy to the conventional 30 m average  $V_s$  ( $V_{s30}$ ). As concerns  $A_d$  and  $A_0$ , theoretical considerations suggest that these parameters are somehow proportional to the amplification effect on the SH component [19], but no direct relationship can be assessed.

Several experimental comparisons between HVSR and various types of site response curves were investigated. Duval et al. [29], Rodríguez and Midorikawa [30] and Haghshenas et al. [18] compared ambient vibrations HVSR with earthquake site-to-reference-spectral-ratio curves. These latter authors, focusing on  $F_0$  and  $A_0$  relationships, considered more refined procedure about ambient vibration processing and acquisition as well as peak reliability check, also analyzing a large dataset from different geological conditions; moreover, they provided a review of studies concerning  $F_0$  and  $A_0$  comparison. Recently, Schleicher and Pratt [31] compared ambient vibration and earthquake HVSR with surface-to-borehole-spectral-ratio curves, also focusing on  $F_0$  and  $A_0$  relationships in a narrow frequency range (about 0.2–3 Hz). Comparison concerning  $F_0$  and  $F_d$  values in a wider range (about 0.4–20 Hz) were explored by Zhu et al. [32] considering earthquake HVSR and surface-to-borehole-spectral-ratios: the amount of data considered and the provided review of the outcomes from different authors, make this contribution a scholar reference for this topic. From these empirical studies, there is a general consensus about the idea that HVSR curve can provide a very good estimate of  $F_0$  value of the site response curve, especially when a sufficiently strong impedance contrast in the subsoil is present. Furthermore, there is an agreement by the authors about the tendency to underestimate  $A_0$  from HVSR maxima. Since the significative lack in the literature concerning  $F_d$  and  $A_d$  comparisons, the relationships with corresponding HVSR peaks are not yet well clarified. Anyway, both Duval et al. [29] and Zhu et al. [32] show a significative tendency by the HVSR in underestimating the  $F_d$  value. Regarding the amplitude differences, it is worth mentioning that some authors (e.g., Refs. [33–35]) point out that an excess of the site response curves can be commonly found for most of the frequencies, attributing as the main cause of this behavior the amplification of the vertical component of the ground motion.

Despite of their intrinsic interest, empirical approaches may be affected by some biases. In fact, as shown by Zhu et al. [32], the identification of the relevant frequency and amplitude parameters may be affected by the procedure used to obtain the HVSR and site response curves (windowing, smoothing, etc.). This bias may be more significant where both HVSR and site response curves present multiple peaks and could be responsible for some heterogeneity among the results obtained by different authors.

To circumvent this issue, theoretical modelling can be an important support. On this purpose, only few works based on a small number of simplified soil profiles exist (e.g., Refs. [17,36]): these studies confirm the agreement between the HVSR and the SH site response curve concerning  $F_0$ , while outcomes regarding the  $A_0$  seem to indicate a dependency of this parameter on some aspects of HVSR modelling.

The aim of the present work is exploring this topic by following a purely 1D theoretical approach, i.e., by comparing outcomes of physical models representative of ambient vibration HVSR and SH site response curves deduced from a standard 1D equivalent linear approach [1,37]. This analysis was accomplished considering a large set of realistic soil profiles. It is worth pointing out that this kind of study cannot substitute the empirical analysis, anyway it may represent an effective benchmark for these last studies.


In the following, the procedure to obtain a large amount of soil profiles used to simulate possible experimental situations is considered at first. Then, the numerical procedures considered for modelling are described. Finally, the results of the comparisons between theoretical HVSR and SH site response curves in terms of  $F_0$ ,  $A_0$ ,  $F_d$  and  $A_d$  values are presented.

## 2 Obtaining soil profiles

The soil profiles taken into account for the numerical simulations result from litho-stratigraphic configurations (hereafter LSCs) obtained from a seismic characterization of geological formations at regional scale (for the details about the framework, see Refs. [38,39]). In particular, each LSC is represented by a specific succession of litho-stratigraphic units (LSUs), each parameterized in terms of thickness and  $V_s$  range of variations. This information was obtained considering data retrieved in Southern Apennines municipalities (Southern Italy) from seismic microzonation studies (<https://www.webms.it>) and from ITACA database [40]. In particular, 175 down-hole seismic tests accompanied by as many geological borehole and outcomes from 195 surface seismic prospecting (surface-wave and refraction investigations) were considered in order to define 8 LSCs (Table 1). From the statistical point of view, these data allow to define topological configurations typical (in the sense of “statistically dominant”) of the considered area and the respective range of variation. Density data is considered as fixed since the respective range of variation is quite small.

alt-text: Table 1

Table 1

 The table layout displayed in this section is not how it will appear in the final version. The representation below is solely purposed for providing corrections to the table. To preview the actual presentation of the table, please view the Proof.

Properties of the eight litho-stratigraphic configurations (LSCs) considered for the generation of the soil profiles used for the numerical simulations. For the meaning of EG units code, see [Supplementary Material 2](#), ASTM [41] and Amanti et al. [42].

LSC	LSU	EG unit	Thickness (m)	$V_s$ (m/s)	Specific weight (KN/m <sup>3</sup> )
LSC1	Sandy silts	ML	2–5	160–260	20
	Gravels	GW	30–50	380–620	20
	Limestones (seismic bedrock)	LPS	$\infty$	800–830	22
LSC2	Conglomerates with sands	GW-GRS	2–55	230–640	20.5
	Clays	COS	78–165	300–799	22
	Clays (seismic bedrock)	COS	$\infty$	800–900	22
LSC3	Weathered/fractured sandstones, marls, argillites, jaspers and marly limestones	SFALS-SFLPS-SFLP-SFCOS	15–20	200–560	22.5
	Sandstones, marls, argillites, jaspers and marly limestones	ALS-LPS-COS	15–25	500–710	22
	Sandstones, marls, argillites, jaspers and marly limestones (seismic bedrock)	ALS-LPS-COS	$\infty$	800–1500	22
LSC4	Sands with gravels and silts	SW	2–20	190–450	19
	Pyroclasts	SM-SW	5–10	500–1200	20
	Lavas	LP-SFLP	5–15	700–1500	22
	Pyroclasts	SM-SW	20–90	500–1200	20
	Alternation of sandstones, argillites, calcarenites and marly clays	AL-ALS	5–25	400–750	22
	Alternation of sandstones, argillites, calcarenites and marly clays (seismic bedrock)	AL-ALS	$\infty$	800–1000	22
LSC5	Weathered/fractured limestones	SFLP	2–8	350–500	22
	Weathered/fractured limestones	SFLP	3–22	500–780	22
	Limestones (seismic bedrock)	LP	$\infty$	820–1500	22
LSC6	Gravels with sands and silts	GM	2–15	160–550	20
	Clays	COS	5–10	200–790	22
	Clays (seismic bedrock)	COS	$\infty$	800–1250	22

LSC7	Weathered/fractured sandstones, sandstones, marls, argillites, jaspers, marly limestones, calcarenites and schists	SFALS-AL-ALS-GRS-COS-LPS	5-30	260-760	22
	Sandstones, marls, argillites, jaspers, marly limestones, calcarenites and schists (seismic bedrock)	AL-ALS-GRS-COS-LPS	$\infty$	800-1500	22
LSC8	Gravels with sands and silts	GM	5-10	120-260	20
	Pyroclasts	SM-SW	15-20	250-640	20
	Alternation of sandstones, argillites, calcarenites and marly clays	AL-ALS	2-5	400-750	22
	Alternation of sandstones, argillites, calcarenites and marly clays (seismic bedrock)	AL-ALS	$\infty$	800-1000	22

These configurations are representative of regional geological domains characterized by different tectonic history and/or depositional modality in a typical chain-foredeep-foreland system. This geological large-scale architecture is entirely present in Southern Apennines and its elements are found throughout the Italian peninsula (see, e.g., Refs. [43,44]). In particular, LSC1, LSC5, LSC3 and LSC7 represent configurations common in chain zones, with the first two existing also in foreland areas; LSC2 and LSC6 are typical successions of foredeep basins, while LSC4 and LSC8 represent configurations belonging to volcanic geological setting. Information characterizing each LSU (Table 1) was codified in terms of engineering-geological units (thereafter EG units, see Refs. [41,42]): this conversion allowed to attribute the geotechnical properties (shear modulus reduction and damping ratio curves as a function of shear strain, as well as specific weight values) to each LSU in the context of 1D equivalent-linear site response simulations. The collected seismic data also allowed to identify the depth range of the seismic bedrock (H), i.e., the reference soil condition for the 1D site response simulations: this layer conventionally corresponds to unweathered rigid soil with  $V_s$  value  $\geq 800$  m/s. In particular, two distinct family of LSCs were defined, one where the seismic bedrock is located at  $H > 30$  m (LSC1, LSC2, LSC3 and LSC4) and the other with  $H < 30$  m (LSC5, LSC6, LSC7 and LSC8).

In order to perform the numerical simulations, 1600  $V_s$  profiles (200 for each LSC, a number considered appropriate in order to capture the estimated  $V_s$  variability) were built by randomizing the relevant thickness and  $V_s$  values characterizing the LSCs by following the Toro [45] model. The randomization process adopted to define the  $V_s$  profiles develops by: 1) generating a sequence of homogeneous layers with thickness varying randomly by following a Poisson distribution with rates decreasing with depth; 2) as function of the depth of the layer barycenter, classifying each layer in terms the EG based on values in Table 1; 3) determining a random  $V_s$  value by considering the values in Table 1 and the correlation with  $V_s$  values relative to the layer immediately above. The parameters controlling the layer thickness variation and the number of  $V_s$  layers were modified case by case in order to obtain profiles compatible with the limit values shown in Table 1. It is appropriate to specify that the number of LSUs does not correspond to that of  $V_s$  layers, but represents the number of strata with different geotechnical properties. The amount of  $V_s$  layers varies from 2 to 35 and also depends on the depth of H; in particular, the average  $V_s$  layer number is 20 and 13 for the LSCs with  $H > 30$  m and  $H < 30$  m respectively. As concerns the  $V_s$  values, a variability characterized by log-normal distribution was assumed and the median ( $\mu$ ) and standard deviation natural logarithm ( $\sigma_{ln}$ ) values were respectively computed in the form:

$$\mu = \sqrt{V_{s_{min}} V_{s_{max}}} \text{ and} \quad (1)$$

Previous Version

$$\sigma_{ln} = \sqrt{\frac{[\ln(V_{s_{min}}) - \ln(\mu)]^2 + [\ln(V_{s_{max}}) - \ln(\mu)]^2}{2}},$$

(2)

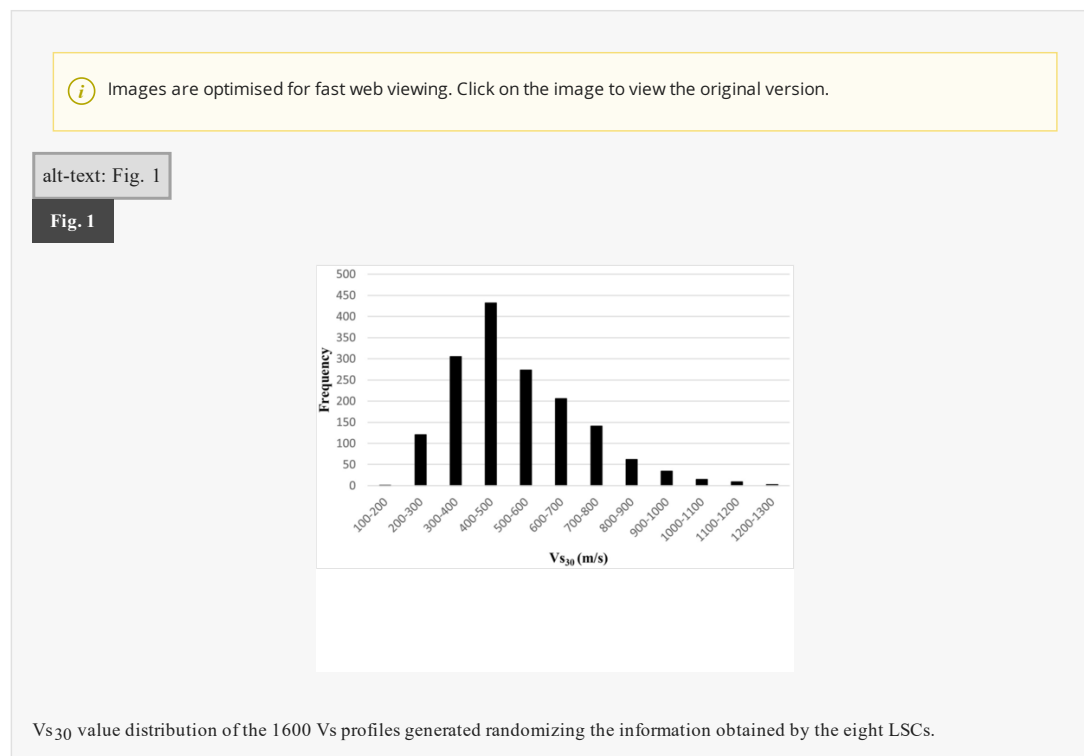
Updated Version

$$\sigma_{ln} = \sqrt{\frac{[\ln(V_{s_{min}}) - \ln(\mu)]^2 + [\ln(V_{s_{max}}) - \ln(\mu)]^2}{2}},$$

where  $V_{s_{min}}$  and  $V_{s_{max}}$  represent the minimum and maximum  $V_s$  value for each LSU, respectively (Table 1). Regarding the inter-layer correlation, the Geomatrix site classification [45] was considered. The possibility of  $V_s$

profiles with non-monotonically increasing trend was included in the randomization procedure. Moreover, it is worth mentioning the case of LSC2: in order to simulate a configuration represented by a deep sedimentary basin with Vs values gradually increasing with depth, the thicker layer of clay (78–165 m) was split in 15–30 m thick sub-layers with a progressive increase of Vs values of 100 m/s. All the generated Vs profiles are collected in numerical format in the [Supplementary Material 1](#); despite the use of the Vs-dependent auto-discretization procedure [3], the output resolution of the layer thickness is always the same for each considered profile.

[Fig. 1](#) shows the distribution of the  $V_{s30}$  values of the 1600 considered profiles. In particular, it is possible to note that these values follow a log-normal distribution, with median value of 494 m/s; similar distribution was detected for real site databases [46,47]. In terms of Eurocode 8 soil classification [48], 122 profiles belong to class A, 1198 to class B and 280 to class C; no class D profiles were generated by the randomization procedure.

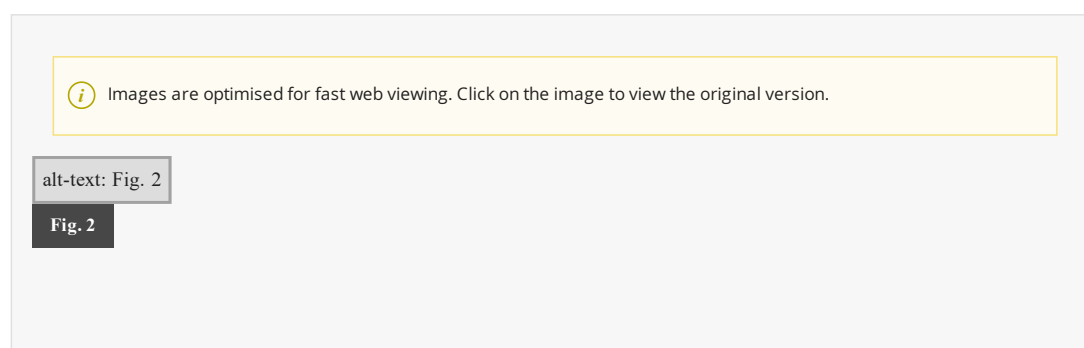


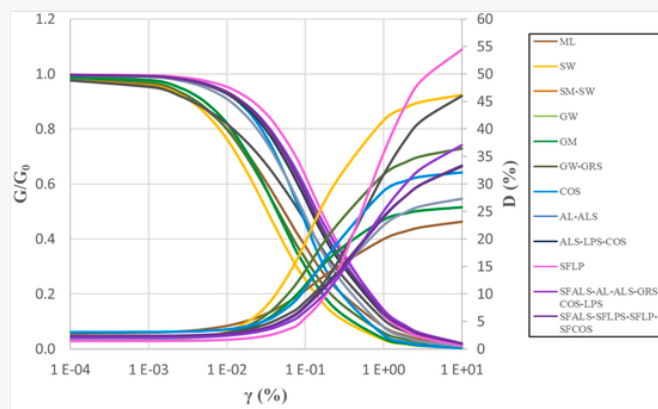
### 3 Numerical simulations

#### 3.1 Simulating acceleration transfer function curves

Site response curves relative to the 1600 profiles were obtained in terms of SH acceleration transfer functions (ATFs) computed in the 1D approximation by means the STRATA code by considering as reference an outcropping reference soil. This site response analysis software was chosen due its wide diffusion in the professional activity.

As concerns the profile geotechnical properties, shear modulus reduction and damping ratio curves as well as specific weight values, were collected through an extensive investigation of the available literature, which summarizes large Italian and international datasets. The list of these specific works and datasets are inserted in the [Supplementary Material 2](#). This information is associated to the relevant EG unit on the basis of the geotechnical description of the samples. In order to obtain the representative decay curves to be used for the simulations ([Fig. 2](#)), those belonging to the same EG unit of the considered LSUs ([Table 1](#)) were averaged together after the regularization using the Yokota et al. [49] model. In LSUs where the EG unit attribution could not be univocal, the representative decay curves are obtained averaging the curves associated to the different possible units. Regarding the characterization of deposits located at depth greater than 50 m, curves by EPRI [50] were considered. Furthermore, curves with constant value of shear modulus and damping ratio (1% and 0.75% respectively) were adopted for the seismic bedrock materials. Finally, the variability associated with the geotechnical properties was reproduced by following Darendeli [51]. All the curves showed in [Fig. 2](#) are collected in numerical format in the [Supplementary Material 2](#).





Representative shear modulus reduction ( $G/G_0$ ) and damping ratio ( $D$ ) curves as a function of shear strain ( $\gamma$ ) of the EG units attributed to each LSU listed in Table 1.

The input ground motion for the reference site condition was determined considering the Italian seismic hazard map ([http://esse1-gis.mi.ingv.it/mps04\\_eng.jsp](http://esse1-gis.mi.ingv.it/mps04_eng.jsp)) relative to the ground motion expected to be exceeded with a probability equal to 10% in 50 years. In particular, seven scaled accelerograms (Table 2) fulfilling the uniform hazard spectrum-compatibility with the zone of the Southern Apennines characterized by  $0.250 \text{ g} < \text{PGA} < 0.275 \text{ g}$ , were selected. It is worth noting that these PGA values are representative of the highest hazard zone in the Italian territory. These natural time-series were extracted from SEISM-HOME Web-GIS (<https://www.eucentre.it/seism-home-accelerograms/?lang=en>; for details, see Ref. [52]).

alt-text: Table 2

Table 2

*i* The table layout displayed in this section is not how it will appear in the final version. The representation below is solely purposed for providing corrections to the table. To preview the actual presentation of the table, please view the Proof.

Characteristics of the seven accelerograms selected for the 1D site response simulations.

Magnitude (Mw)	Epicentral Distance (Km)	PGA (g)	Scaling factor (%)	File name
6.87	11.00	0.263	0.78	ESD 000182xa.cor
6.68	65.00	0.263	1.16	ESD 000200xa.cor
6.93	94.31	0.263	2.84	NGA 0797y.txt
6.69	38.07	0.243	1.73	NGA 1091x.txt
6.60	36.18	0.263	2.07	KNET1 SAG0010503201053.NS
6.00	33.00	0.212	2.00	ITACA 19780415_233347ITDPC_NAS__WEC.DAT
6.30	50.42	0.263	0.44	ITACA 20090406_013239ITDPC_SBC__WEC.DAT

Overall, a set of seven ATFs for each profile were obtained and the median curve, defined in the frequency range 0.1–30 Hz, was chosen as the profile-representative one.

### 3.2 Simulating HVSR curves

Horizontal to Vertical Spectral Ratio curves were simulated using full wavefield ambient vibrations models. Since all the seismic phases (surface and body waves) can play an important role in defining the HVSR curve [53], the use of this kind of simulation approaches was preferred in this study to the models based on the contribution of specific phases only (e.g., Refs. [54,55]). In particular, two different full wavefield models were considered: one based on Distributed Surface Sources hypothesis (DSS in the following), and the other based on the Diffuse Field Approach (DFA in the following). In the frame of DSS assumption, the model proposed by Lunedei and Albarello [56,57] was considered: in this approach, the ambient vibration wavefield is accounted as the effect of a random uniform distribution of spatially-

correlated sources located at the surface of the Earth. On the contrary, the DFA model (e.g., Refs. [58,59]), following the assumption that ambient vibration is a diffuse random wavefield, removes the role of sources linking the simulated HVSR curve exclusively with the effect of the subsoil local structure. In particular, the routine described by García-Jerez et al. [60] and available at <https://w3.ual.es/GruposInv/hv-inv/> was used for this work. Beyond these main aspects, a more detailed theoretical comparison between the two models was made by Lunedei and Malischewsky [61]. It is worth mentioning that DSS model includes the effects of material damping, while DFA model is purely elastic.

HVSR curve was simulated for the 1600 Vs profiles with both models in the range 0.1–30 Hz. Compressional wave velocity ( $V_p$ ) values are computed assuming a value of 0.4 for the Poisson's ratio and density values were deduced from  $V_p$  values following the relationships proposed by Brocher [62]. For DSS model, the two horizontal and the vertical input components of displacement were assumed to be equal to each other; furthermore, damping values for  $V_p$  and Vs are assumed equal to 0.01 for all the layers. For both models, ten modes for surface waves (Rayleigh and Love) were considered and the HVSR curve was computed as


$$HVSR = \sqrt{\frac{2P_H}{P_V}}, \quad (3)$$

where  $P_H$  and  $P_V$  are the power spectra density of the ambient-vibration ground-motion horizontal component and vertical component, respectively.

Of course, illustrating the different role of some parameters on the HVSR pattern (Poisson's ratio, density and damping values), in the assumption that such analysis is able to account all possible configurations of the subsoil, would be of theoretical interest but well beyond the scope of the present work. For this reason, realistic values were simply chosen for these parameters.

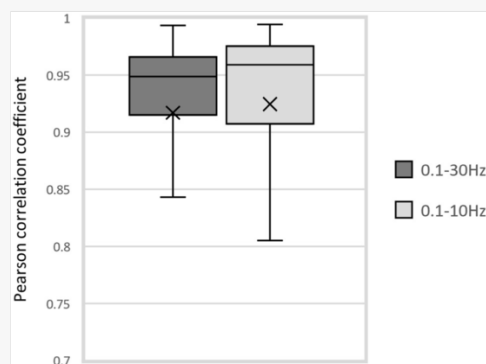
## 4 Comparison outcomes

As a first analysis, each HVSR curve obtained by the DSS model was compared with the relevant one computed using the DFA model in order to check if significant differences exist between the resulting HVSR patterns. To this purpose, Pearson correlation coefficients were computed considering the range 0.1–30 Hz (Fig. 3): their value distribution shows an overall high correlation between the two HVSR, with the median and mean values equal to 0.95 and 0.92, respectively. The same analysis was performed considering the curves in the range 0.1–10 Hz, obtaining very similar median and mean values (0.96 and 0.93, respectively) with a slightly wider interquartile range. In view of these outcomes, each of the two models could be considered as representative of HVSR data. For sake of simplicity, only one model was taken into account: on the basis of its possibility of modelling the material damping, the choice fell on DSS model.

 Images are optimised for fast web viewing. Click on the image to view the original version.

alt-text: Fig. 3

Fig. 3




Box and whisker plot showing the distribution of the Pearson correlation coefficient values computed comparing the HVSR curves obtained by DSS and DFA model considering the frequency range 0.1–30 Hz (dark grey) and 0.1–10 Hz (light grey). Each box represents the interquartile range; the median value is represented by the horizontal black line within the box, while the mean value is represented by the cross. The whiskers are lines that extend from the lower and upper edge of the box to the 5th and 95th percentile of the distribution, respectively.

By using this information,  $F_0$  and  $F_d$  values along with the relevant  $A_0$  and  $A_d$  values were picked up from HVSR and ATF curves. Since theoretical curves were used, no significance criterion (e.g., Ref. [63]) was adopted in detecting



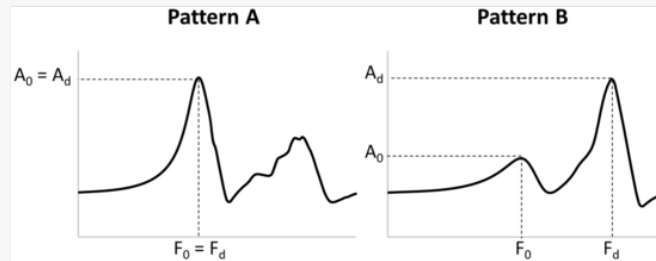
their representative peaks.

In order to obtain additional information about the general trends of both curves, two distinct patterns are identified (Fig. 4): pattern A, where  $F_0$  corresponds to  $F_d$  (and therefore  $A_0$  coincides to  $A_d$ ), and pattern B, where  $F_0$  and  $F_d$  values (and therefore  $A_0$  and  $A_d$ ) are associated with different peaks. Obviously, unlike the schematic patterns in Fig. 4, the simulated curves can be characterized by more than two peaks.

 Images are optimised for fast web viewing. Click on the image to view the original version.

alt-text: Fig. 4

Fig. 4




Representative scheme of the two patterns characterizing the theoretical curves. Pattern A (on the left), where  $F_0 = F_d$  (and  $A_0 = A_d$ ); pattern B (on the right), where  $F_0 \neq F_d$  (and  $A_0 \neq A_d$ ).

As concerns the HVSR curves, pattern A represents 86% of the total: very similar percentage (about 85%) are found by Zhu et al. [32] considering empirical HVSR data. No simple relationship between the  $V_s$  profile and the shape of the HVSR curve can be easily found. In general, the relationship between the shape of the HVSR curve and the  $V_s$  profile is highly non-linear due to the complex wave propagation patterns generated by  $V_s$  variations within the considered profile. One can expect that the effect of each layer on the HVSR curve may depend on its thickness and on the  $V_s$  difference with close layers. Moreover, the HVSR value at any frequency is expected to depend on the combined effects of different impedance contrasts in the  $V_s$  profile and, eventually, on the presence and respecting number of  $V_s$  reversals. The number of possible combinations (see the considered profiles provided in the Supplementary Material 1) is very large and would require analyses that are well beyond the target of the present work, which is mainly devoted to provide practitioners with a warning about the possible interpretation of the HVSR curve as representative of the 1D seismic response. Just to give some number, in the hypothesis that a “significant” HVSR peak is characterized by amplitude values above 1.2 (to say) and that a  $V_s$  impedance contrast is considered as “significant” if related to a change of 50% of the  $V_s$  value, curves with a single peak, two peaks and more than two peaks represent 55%, 38% and 7% of the total respectively. Furthermore, one can see that HVSR curves having a single peak are associated to a single significant impedance contrast in 56% of cases only. For 9% of cases there is not any significant contrast and in 32% two impedance contrasts are present; in the remaining 2% of cases more than two impedance contrasts exist (see Table 3). This prevents any simple physical interpretation of the HVSR profiles as a function of the impedance contrasts.

alt-text: Table 3

Table 3

 The table layout displayed in this section is not how it will appear in the final version. The representation below is solely purposed for providing corrections to the table. To preview the actual presentation of the table, please view the Proof.

Percentage of configurations in terms of  $V_s$  “significant” impedance contrasts (above 50% of respective  $V_s$  values) as function of the number of “significant” HVSR maxima (amplitude values above 1.2).

	No. of HVSR maxima		
	1	2	>2
0	9	6	12
1	56	38	41
2	32	52	44
>2	2	4	3

Regarding ATF curves, pattern A is 72% of the total: this means that a number of cases where HVSR pattern A coincides with ATF pattern B (hereafter cases AB) and vice-versa (hereafter cases BA) can exist. Outcomes of this comparison are shown in Table 4. As a whole, the pattern agreement (cases AA + BB) is verified in 68% of cases; most misidentifications (23%) concern AB cases.

alt-text: Table 4

Table 4

*i* The table layout displayed in this section is not how it will appear in the final version. The representation below is solely purposed for providing corrections to the table. To preview the actual presentation of the table, please view the Proof.

Percentage distribution of the pattern comparison between HVSR and ATF curves.

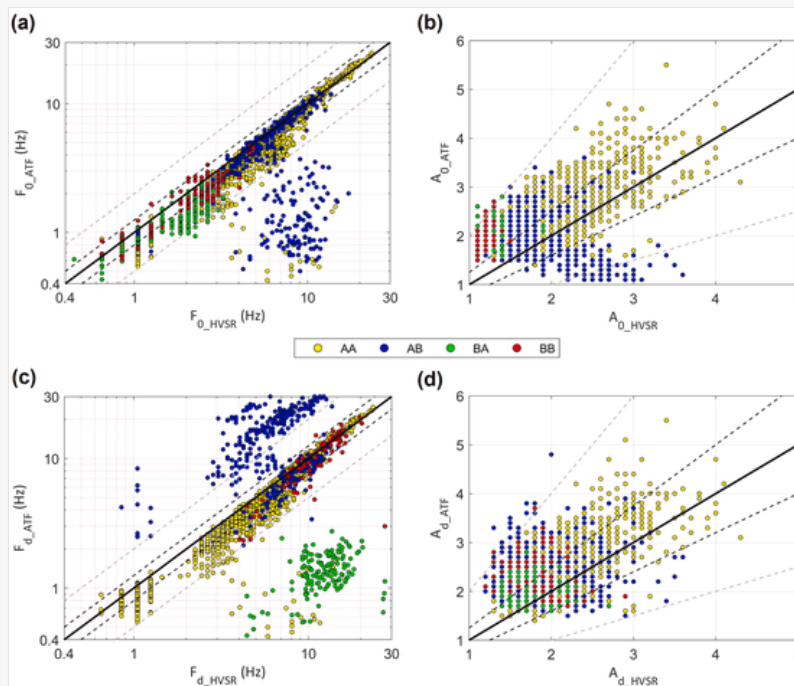
		ATF	
		A	B
HVSR	A	63	23
	B	9	5

The comparisons between  $F_0$ ,  $A_0$ ,  $F_d$  and  $A_d$  values for HVSR ( $F_{0\_HVSR}$ ,  $A_{0\_HVSR}$ ,  $F_{d\_HVSR}$  and  $A_{d\_HVSR}$ ) and ATF ( $F_{0\_ATF}$ ,  $A_{0\_ATF}$ ,  $F_{d\_ATF}$  and  $A_{d\_ATF}$ ) curves are shown in Fig. 5. The strength of the correlations is estimated considering Pearson, Spearman and Kendall coefficients. Unlike the first, adopted for a direct comparison with other studies (e.g., Ref. [32]), Spearman and Kendall coefficients were also implemented since they do not require normally distributed data and are insensitive to outliers. Moreover, as proposed by Zhu et al. [32], to quantify how the comparisons deviate from 1:1 line, the benchmarks marked by the lines where the ratios  $F_{ATF}/F_{HVSR}$  (and  $A_{ATF}/A_{HVSR}$ ) are equal to 0.5, 0.8, 1.25, and 2 were adopted. Percentages of cases outside these boundaries (hereafter also referred to as “outliers”) along with the correlation coefficient values are summarized in Table 5.

*i* Images are optimised for fast web viewing. Click on the image to view the original version.

alt-text: Fig. 5

Fig. 5



Scatterplots for  $F_0$  (a),  $A_0$  (b),  $F_d$  (c) and  $A_d$  (d) values belonging to the HVSR-ATF comparison. Yellow, blue, green and red dots correspond to cases AA, AB, BA and BB respectively. The solid black line represents the 1:1 line, black and grey dashed lines delimit the benchmark range  $0.8 < F_{ATF}/F_{HVSR} < 1.25$  (or  $0.8 < A_{ATF}/A_{HVSR} < 1.25$ ) and  $0.5 < F_{ATF}/F_{HVSR} < 2$  (or  $0.5 < A_{ATF}/A_{HVSR} < 2$ ), respectively.

alt-text: Table 5

Table 5

*i* The table layout displayed in this section is not how it will appear in the final version. The representation below is solely purposed for providing corrections to the table. To preview the actual presentation of the table, please view the Proof.

Values of the considered correlation coefficients and percentages of the profiles outside the proposed benchmarks for  $F_0$ ,  $F_d$ ,  $A_0$  and  $A_d$  values belonging to HVSR-ATF comparison.

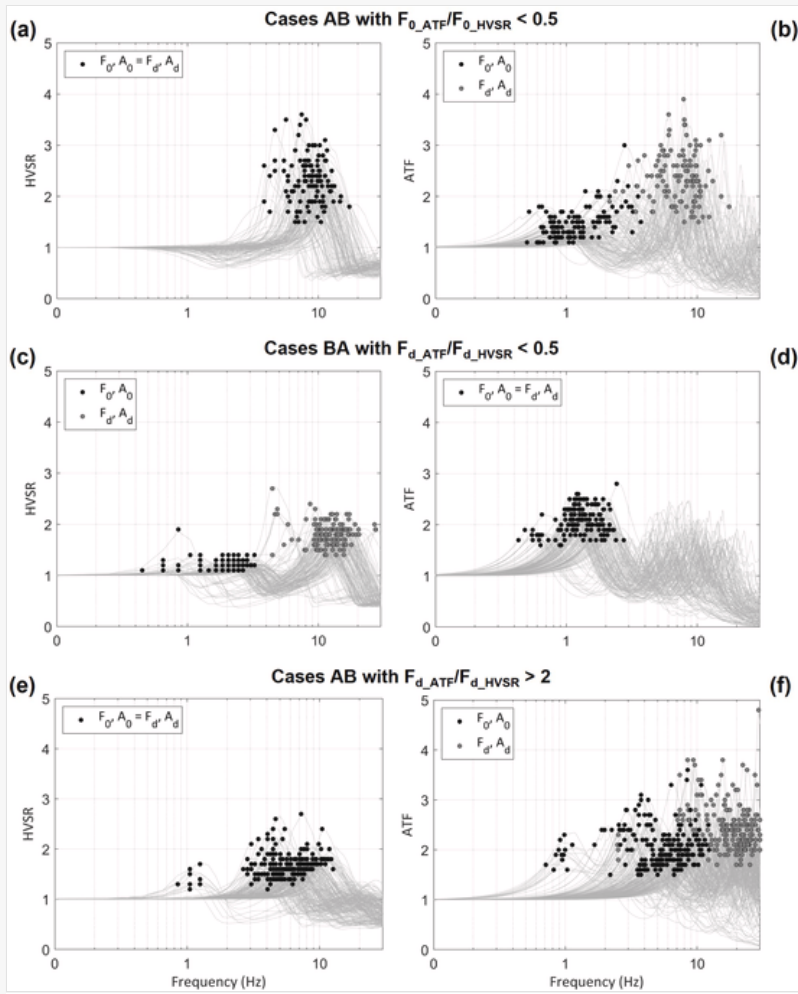
	$F_0$	$F_d$	$A_0$	$A_d$
<b>Pearson correlation coefficient</b>	0.85	0.44	0.51	0.51
<b>Spearman correlation coefficient</b>	0.76	0.54	0.47	0.42
<b>Kendall correlation coefficient</b>	0.68	0.46	0.36	0.31
<b>% where <math>F(\text{or } A)_{ATF}/F(\text{or } A)_{HVS} &lt; 0.8</math></b>	40	33	7	4
<b>% where <math>F(\text{or } A)_{ATF}/F(\text{or } A)_{HVS} &gt; 1.25</math></b>	–	15	41	41
<b>% where <math>F(\text{or } A)_{ATF}/F(\text{or } A)_{HVS}</math> out of range [0.8–1.25]</b>	40	49	48	45
<b>% where <math>F(\text{or } A)_{ATF}/F(\text{or } A)_{HVS} &lt; 0.5</math></b>	10	11	2	–
<b>% where <math>F(\text{or } A)_{ATF}/F(\text{or } A)_{HVS} &gt; 2</math></b>	–	13	1	1
<b>% where <math>F(\text{or } A)_{ATF}/F(\text{or } A)_{HVS}</math> out of range [0.5–2]</b>	10	25	3	1

As concerns the peak frequency comparisons (Fig. 5a and 5c), a better agreement for  $F_0$  is evident. In particular, the percentages of the profiles out of the ranges  $0.8 < F_{0\_ATF}/F_{0\_HVS} < 1.25$  and  $0.5 < F_{0\_ATF}/F_{0\_HVS} < 2$  are 40% and 10% respectively: slightly lower values (31% and 8%) and a very similar Pearson coefficient estimate (0.89) were found by Zhu et al. [32] analysing the comparison between HVSR and surface-to-borehole-spectral-ratio curves. Contrary to the outcomes shown by these authors for  $F_0$  values, the outliers are exclusively located below the bound where  $F_{0\_ATF}/F_{0\_HVS} = 0.8$ . Moreover, it is worth noting that the outliers with  $F_{0\_ATF}/F_{0\_HVS} < 0.5$  are mostly represented by part of the cases AB. In these cases, where  $F_{0\_HVS}$  strongly overestimates  $F_{0\_ATF}$ , it is possible to note that both curves are instead characterized by similar  $F_d$  estimates (Fig. 6a and b), whose values are located close to the 1:1 line (most within the range  $0.8 < F_{d\_ATF}/F_{d\_HVS} < 1.25$ , Fig. 5c). This demonstrates that the  $F_{0\_ATF}$  peak is not reproduced by HVSR modelling in these configurations, as can be noted observing Fig. 6a and 6b: in particular, this characteristic can occur for  $F_{0\_ATF}$  values ranging from 0.4 to 3 Hz.

*i* Images are optimised for fast web viewing. Click on the image to view the original version.

alt-text: Fig. 6

Fig. 6



HVS curves simulated using the DSS model (a, c, e) and ATF curves (b, d, f) belonging to the cases AB with  $F_{0\_ATF}/F_{0\_HVS} < 0.5$  (a, b), BA with  $F_{d\_ATF}/F_{d\_HVS} < 0.5$  (c, d) and AB with  $F_{d\_ATF}/F_{d\_HVS} > 2$  (e, f). Black dots are the peaks defined by  $F_0$  and  $A_0$ , the grey ones by  $F_d$  and  $A_d$ . The curves with only black dots ( $F_0 = F_d, A_0 = A_d$ ) belong to the pattern A, those with both dots ( $F_0 \neq F_d, A_0 \neq A_d$ ) belong to the pattern B.


Regarding the  $F_d$  comparison, the percentages of the cases out of the ranges  $0.8 < F_{d\_ATF}/F_{d\_HVS} < 1.25$  and  $0.5 < F_{d\_ATF}/F_{d\_HVS} < 2$  are greater than those (40% and 16%) found by Zhu et al. [32], whose outliers show only an underestimate of the  $F_d$  of the site response curve by HVS. In this analysis, the possibility of both underestimating and overestimating by Horizontal to Vertical Spectral Ratios emerges from the outcomes: in particular, outliers with  $F_{d\_ATF}/F_{d\_HVS} > 2$  correspond to part of cases AB, those where  $F_{d\_ATF}/F_{d\_HVS} < 0.5$  mainly to cases BA (Fig. 5c). Since the nature of the cases, it is evident that these differences in  $F_d$  estimates are related to the respective relationships between  $A_0$  and amplitude values of higher frequency peaks. In particular, the first and second amplitude values are underestimated by HVS modelling in cases BA (Fig. 6c and 6d) and AB (Fig. 6e and 6f) respectively. Despite of the clear relationships between the HVS and ATF patterns in these two groups of outliers, it was not possible to identify

any type of diagnostic element in HVSR curves (e.g., specific differences/ratios between  $A_{0\_HVS\!R}$  and  $A_{d\_HVS\!R}$  or between  $A_{0\_HVS\!R}$  and amplitude of second higher amplitude peak) capable of identifying these situations in advance. Thus, it is reasonable to suppose that these cases can be related with some specific  $V_s$  profiles or particular combination of the latter with certain decay curves. However, this kind of investigation is beyond the aim of this study.

As concerns the peak amplitude values (Fig. 5b and 5d),  $A_0$  and  $A_d$  comparisons are characterized by a very similar agreement around the 1:1 line and analogous correlation characteristics (Table 5). In particular, it is possible to note that most outliers are included in the benchmark range  $1.25 < A_{ATF}/A_{HVS\!R} < 2$ : this means that the HVSR curve tends to slight underestimate at a similar extent  $A_{0\_ATF}$  and  $A_{d\_ATF}$  values. This feature univocally characterizes  $A_{0\_ATF}$  estimates by the HVSR curves belonging to the pattern B (Fig. 5b), which refer to lower  $F_{0\_HVS\!R}$  range (0.5–4 Hz) than pattern A (Fig. 5a). Still regarding  $A_0$  comparison, it is worth mentioning the characteristics of the cases where  $A_{0\_ATF}/A_{0\_HVS\!R} < 0.8$  (Fig. 5b), in which  $A_{0\_ATF}$  is overestimated: these outliers, which mainly represent cases AB, correspond to the same cases characterized by  $F_{0\_ATF}/F_{0\_HVS\!R} < 0.5$  (Fig. 5a; Fig. 6a and b). Considering that they are associated with  $A_{0\_ATF}$  values in the range 1–2, this suggests that the non-reproducibility of the  $F_{0\_ATF}$  peak for these profiles by HVSR modelling is related with very low impedance contrasts.

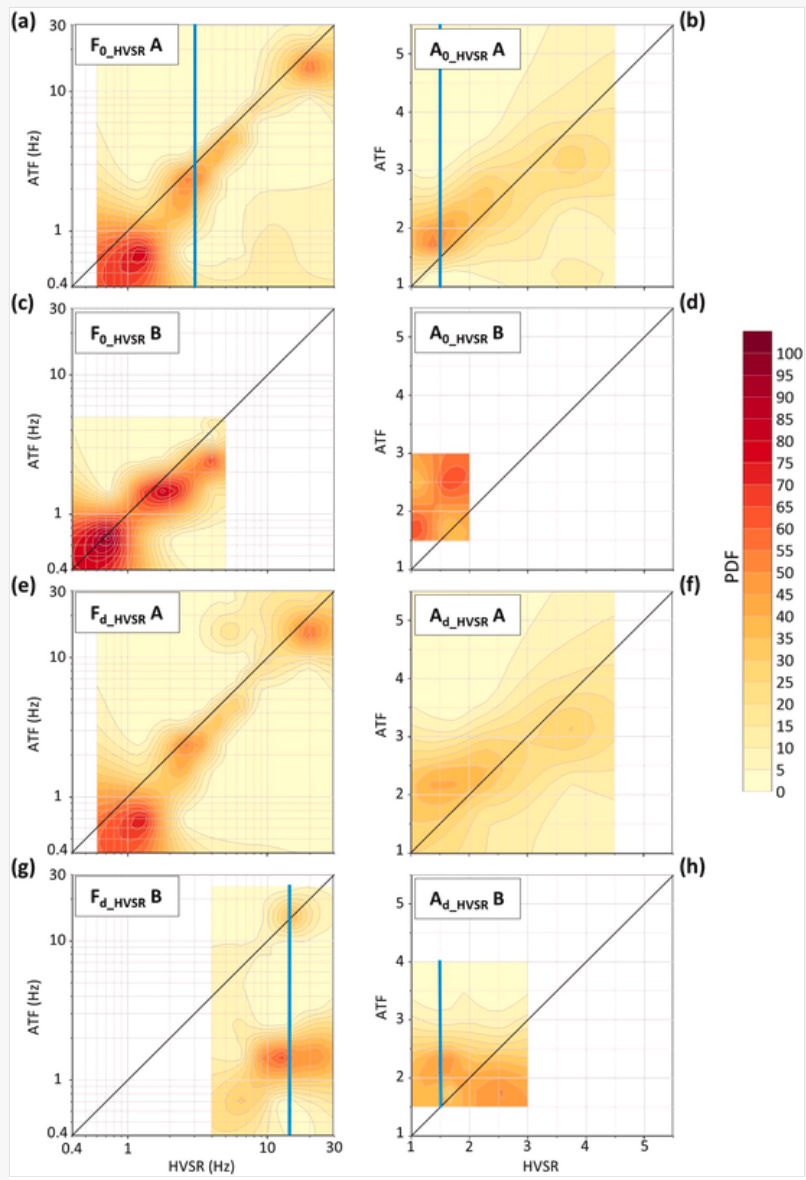
## 5 Probability density function analysis

Information obtained from the outcomes discussed above were considered to define the degree of reliability of ATF peak estimates provided by HVSR curves. To perform this analysis, the probability density functions (PDFs) of the  $F_{0\_ATF}$ ,  $A_{0\_ATF}$ ,  $F_{d\_ATF}$  and  $A_{d\_ATF}$  values as a function of the relevant HVSR estimates were computed using Kriging interpolation algorithm (Fig. 7). In particular, PDF of ATF values were computed considering separately HVSR pattern A and B: in this way, one can assess the correctness probability provided by the HVSR peak parameters considering the position of the maximum amplitude peak in this curve (pattern A or B). As can be seen in Fig. 7, the interpolation area is not equivalent for all the cases: the procedure concerned exclusively the frequency or amplitude range where the theoretical values have been actually determined (Fig. 5), thus avoiding significant extrapolations. Observing some representative PDF sections carried out considering certain  $F_{0\_HVS\!R}$ ,  $A_{0\_HVS\!R}$ ,  $F_{d\_HVS\!R}$  and  $A_{d\_HVS\!R}$  values belonging to specific patterns (Fig. 8), it is possible to note unimodal and bimodal distributions of the corresponding PDF of ATF values. In particular, considering a HVSR pattern A curve with  $F_{0\_HVS\!R}$  equal to 3 Hz (Fig. 8a), we can observe a bimodal distribution with a high probability to obtain an  $F_{0\_ATF}$  value around 2.5 Hz (that is, close to HVSR estimate) and a significantly lower probability to have a value at about 0.4 Hz. This means that the  $F_{0\_ATF}$  estimate via HVSR is characterized by a low probability of failing significantly at this frequency. A different situation is shown for a HVSR pattern B curve with  $F_{d\_HVS\!R}$  equal to 14.5 Hz (Fig. 8c): in this case, the PDF of  $F_{d\_ATF}$  values shows a clear bimodal distribution with a higher probability to drastically fail the estimate via HVSR (the highest PDF maxima is centered at about 1.5 Hz) than to fulfill it. As concerns the peak amplitudes, for a HVSR pattern A curve with  $A_{0\_HVS\!R}$  equal to 1.5 (Fig. 8b), the clear unimodal PDF distribution centered at about 1.8 shows a high probability to slightly fail the estimate; a similar behavior is showed for HVSR pattern B curve with  $A_{d\_HVS\!R}$  equal to 1.5 (Fig. 8d), where the higher PDF peak is located at  $A_{d\_ATF}$  about 2.5.


 Images are optimised for fast web viewing. Click on the image to view the original version.

alt-text: Fig. 7

Fig. 7

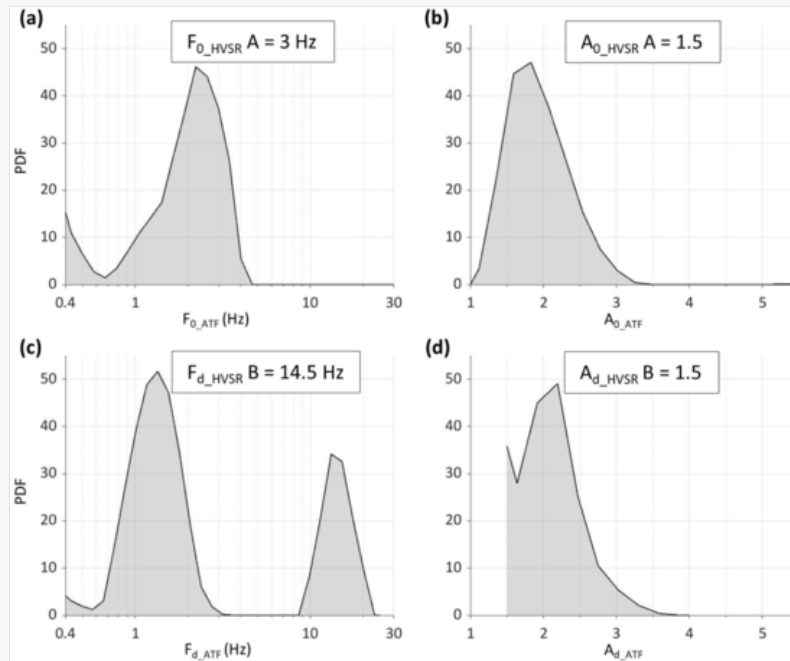


Probability density functions (PDFs) of  $F_{0\_ATF}$  (a, c),  $A_{0\_ATF}$  (b, d),  $F_{d\_ATF}$  (e,g) and  $A_{d\_ATF}$  (f, h) values as a function of the relevant HVSR estimates obtained by DSS model. PDFs were computed considering separately HVSR pattern A (a, b, e, f) and B (c, d, g, h), while both patterns were considered together for ATF in all the analyses. The solid black lines represent the 1:1 lines, while the blue ones are the traces of the PDF sections showed in Fig. 8.

 Images are optimised for fast web viewing. Click on the image to view the original version.

alt-text: Fig. 8

Fig. 8



Representative sections of some PDF plots showed in Fig. 7. In particular, section (a) shows PDF of  $F_{0\_ATF}$  values obtained for HVSR pattern A curve with  $F_{0\_HVSR} = 3$  Hz (trace in Fig. 7a); section (b) shows PDF of  $A_{0\_ATF}$  values obtained for HVSR pattern A curve with  $A_{0\_HVSR} = 1.5$  (trace in Fig. 7b); section (c) represents PDF of  $F_{d\_ATF}$  values considering a HVSR pattern B curve with  $F_{d\_HVSR} = 14.5$  Hz (trace in Fig. 7g); section (d) represents PDF of  $A_{d\_ATF}$  values considering a HVSR pattern B curve with  $A_{d\_HVSR} = 1.5$  (trace in Fig. 7h).

## 6 Conclusions

The use of a large number of numerical simulations allowed to compare theoretical ambient vibration HVSR curves and respective ATF curves. This comparison is performed by considering their representative peak parameter values, that is  $F_0$ ,  $A_0$ ,  $F_d$  and  $A_d$ . Outcomes of the comparisons clearly show that HVSR is a reliable proxy for  $F_0$ , thus confirming what was observed with the empirical studies. Nevertheless, a number of misidentifications of  $F_{0\_ATF}$  values can occur for very low impedance contrasts related to relative low frequency range (0.4–3 Hz). On the other hand, HVSR curve is a less effective proxy as concerns  $F_d$  values, where a significant number of strong underestimates and overestimates occur. In particular, the first situation, also identified by empirical works [29,32], is

associated with an amplitude underestimation of frequency peaks higher than  $F_0$  by HVSR; the second one is instead related to an  $A_0$  underestimation. In order to confirm these last results,  $F_d$  comparison should be explored by further experimental analysis, especially using ambient vibration HVSR.

Outcomes concerning peak amplitude values show a tendency by HVSR to underestimate in a similar way both  $A_{0\_ATF}$  and  $A_{d\_ATF}$  values: this feature is also in agreement with what emerges from empirical comparison concerning  $A_0$  values. In particular, the extent of this amplitude underestimation (between 20% and 50%) is comparable with the results showed by Haghshenas et al. [18] in the amplitude range (about 1–5) analyzed in this work. Moreover, these findings are in line with the general amplitude underestimation by HVSR curve showed by other experimental works [33–35].

Finally, PDF analysis allowed to evaluate for which of these representative parameters the HVSR estimates are affected by high probability to significantly fail. This characteristic especially occurs for the  $F_{d\_ATF}$  estimate via HVSR pattern B curve for the frequency range 10–30 Hz (Fig. 7g), where a high probability (pointed out by PDF values higher than 50%) to overestimate the value more than 200% exists. This information can be of great help in site classification schemes where  $F_d$  value is a primary site amplification proxy (e.g., Refs. [23,24,26]). On the contrary, despite the significant number of outliers (the cases AB in Fig. 5a and 5c), HVSR pattern A curve is characterized by low probability to significantly fail  $F_0$  and  $F_d$  assessments: in fact, in the frequency range where these incorrect estimates can occur (about 6–15 Hz for  $F_0$  and 3–15 Hz for  $F_d$ ), PDF values are lower than 20% (Fig. 7a and 7e). Regarding peak amplitude values, it is possible to note that the highest PDF values are located in the proximity of the 1:1 line in all the situations, highlighting a high probability from the HVSR to slightly underestimate the ATF values (Fig. 7b, Fig. 7d, Fig. 7f and Fig. 7h). Only for HVSR pattern B curve a high probability to slightly overestimates  $A_{d\_ATF}$  values exists (Fig. 7h).

Some final statements concern the limitations of the present study. First of all, outcomes derive from numerical experiments and no attempt is performed to check their validity with new observations. On one side, this approach allows exploring a large set of subsoil configurations which is not possible when empirical data are considered. Anyway, our results appear in line with those provided by empirical studies: in this perspective, our findings can be considered a generalization of experimental studies. Secondly, no physical interpretation is here attempted of HVSR shapes as a function of  $V_s$  profile characteristics. Due to the complex non-linear relationship between these two features, any physical interpretation is only possible when very simple  $V_s$  profiles are considered (e.g., Ref. [19]). As a consequence, eventual sensitivity analyses concerning the role of single parameters (layering, damping, etc.), if any way possible, would require devoted studies. This has not been performed here since the aim was providing practitioners with warnings and simple tools to evaluate at what extent, in realistic complex situations, the HVSR curve and in particular its maxima, may provide useful rules-of-the-thumb to retrieve indications about the corresponding transfer function. On the contrary, sensitivity studies will result mandatory when inversion protocols are of concern, which is not the present case (e.g., Ref. [21]).

## 7 Data and resources

The geognostic and seismic data of Southern Apennines municipalities (Southern Italy) were retrieved from seismic microzonation studies (<https://www.webms.it/>; last accessed on July 17, 2022) and from ITACA database ([http://itaca.mi.ingv.it/ItacaNet\\_31/#/home](http://itaca.mi.ingv.it/ItacaNet_31/#/home); last accessed on July 17, 2022). The STRATA code (release 0.8.0, doi 10.5281/zenodo.3714128) was downloaded from <https://github.com/arkottke/strata/releases> (last accessed on July 17, 2022). The input time-series listed in Table 2 were extracted from <https://www.eucentre.it/seism-home-accelerograms/?lang=en> (last accessed on July 17, 2022). The routine simulating HVSR following DFA model was downloaded from <https://w3.ual.es/GruposInv/hv-inv/> (last accessed on July 17, 2022). Supplementary Material 1 collects the 1600  $V_s$  profiles generated by the randomization procedure; Supplementary Material 2 includes the Engineering-Geological (EG) unit description (Table 1), the decay curves in numerical format (Fig. 2) and the list of specific works and datasets from which these curves were obtained.

## Author contributions

**Enrico Paolucci:** Conceptualization, Methodology, Software, Formal analysis, Writing - Original Draft, Visualization.

**Anna Tanzini:** Software, Formal analysis, Data Curation, Writing - Review & Editing, Visualization.

**Dario Albarello:** Conceptualization, Writing - Review & Editing, Supervision.

## Declaration of competing interest

The authors declare that they have no known competing financial interests or personal relationships that could have appeared to influence the work reported in this paper.

## Acknowledgements




We are grateful to Dr. Enrico Lunedei and Dr. Antonio García-Jerez for the precious and useful suggestions concerning the HVSR numerical simulations. Moreover, many thanks are due to the three anonymous referees whose suggestions helped us to significantly improve the original manuscript.

## Appendix A Supplementary data

Supplementary data to this article can be found online at <https://doi.org/10.1016/j.soildyn.2022.107703>.

## References

 The corrections made in this section will be reviewed and approved by a journal production editor. The newly added/removed references and its citations will be reordered and rearranged by the production team.

- [1] Kramer S.L. Geotechnical earthquake engineering. New Jersey, NJ, USA: Prentice Hall; 1996.
- [2] Boore D.M., Survey U.S.G. SMSIM--Fortran programs for simulating ground motions from earthquakes: Version 2.0.--a revision of OFR 96-80-A. 2000. doi:10.3133/ofr00509. vVersion 2.18. Reston, VA.
- [3] Kottke A., Rathje E. Technical manual for strata. Report No.: 2008/10. Pacific earthquake engineering research center. Berkeley: University of California; 2008.
- [4] Ordonez G. SHAKE 2000: a computer program for the 1-D analysis of geotechnical earthquake engineering problems. Washington, USA: Lacey; 2012.
- [5] WGSM (Working Group on Seismic Microzoning) . Indirizzi e criteri per la microzonazione sismica. Rome, Italy: conferenza delle Regioni e delle Province autonome – Dipartimento della Protezione Civile . (in Italian) <https://www.centromicrozonazioneismica.it/it/download/category/7-indirizzi-e-criteri-per-la-microzonazione-sismica> , 2008 <https://www.centromicrozonazioneismica.it/it/download/category/9-guidelines-for-seismic-microzonation> (English version).
- [6] Albarello D. Extensive application of seismic microzoning in Italy: methodological approaches and socio-political implications. Boll Geofis Teor Appl 2017;58. doi:10.4430/bgta0205.
- [7] Moscatelli M., Albarello D., Scarascia Mugnozza G., Dolce M. The Italian approach to seismic microzonation. Bull Earthq Eng 2020;18:5425–5440. doi:10.1007/s10518-020-00856-6.
- [8] Bard P.-Y. Microtremor measurements: a tool for site effect estimation? Second International Symposium on the effects of surface geology on seismic motion 1999;3:1251–1279.
- [9] Nakamura Y. What is the Nakamura method? Seismol Res Lett 2019;90:1437–1443. doi:10.1785/0220180376.
- [10] Molnar S., Sirohey A., Assaf J., Bard P.-Y., Castellaro S., Cornou C., et al. A review of the microtremor horizontal-to-vertical spectral ratio (MHVSR) method. J Seismol 2022. doi:10.1007/s10950-021-10062-9.
- [11] Bour M., Fouissac D., Dominique P., Martin C. On the use of microtremor recordings in seismic microzonation. Soil Dynam Earthq Eng 1998;17:465–474. doi:10.1016/S0267-7261(98)00014-1.
- [12] Molnar S., Assaf J., Sirohey A., Adhikari S.R. Overview of local site effects and seismic microzonation mapping in Metropolitan Vancouver, British Columbia, Canada. Eng Geol 2020;270:105568. doi:10.1016/j.enggeo.2020.105568.
- [13] Régnier J., Bertrand E., Cadet H. Repeatable process for seismic microzonation using 1-D site-specific response spectra assessment approaches. Application to the city of Nice. France. Eng Geol 2020;270:105569. doi:10.1016/j.enggeo.2020.105569.
- [14]

- [15] Giallini S., Paolucci E., Sirianni P., Albarello D., Gaudiosi I., Polpetta F., et al. Reconstruction of a reference subsoil model for the seismic microzonation of Gori (Georgia): a procedure based on principal component analysis (PCA). *Bull Seismol Soc Am* 2021;111. doi:10.1785/0120200341.1921–39.
- [16] Parolai S., Bormann P., Milkereit C. New relationships between Vs, thickness of sediments, and resonance frequency calculated by the H/V ratio of seismic noise for the cologne area (Germany). *Bull Seismol Soc Am* 2002;92:2521–2527. doi:10.1785/0120010248.
- [17] Bonnefoy-Claudet S., Cornou C., Bard P.-Y., Cotton F., Moczo P., Kristek J., et al. H/V ratio: a tool for site effects evaluation. Results from 1-D noise simulations. *Geophys J Int* 2006;167:827–837. doi:10.1111/j.1365-246X.2006.03154.x.
- [18] Haghshenas E., Bard P.-Y., Theodulidis N., SESAME WP04 Team. Empirical evaluation of microtremor H/V spectral ratio. *Bull Earthq Eng* 2008;6:75–108. doi:10.1007/s10518-007-9058-x.
- [19] Lunedei E., Albarello D. Theoretical HVSR curves from full wavefield modelling of ambient vibrations in a weakly dissipative layered Earth. *Geophys J Int* 2010. doi:10.1111/j.1365-246X.2010.04560.x.
- [20] Oubaiche E.H., Chatelain J., Hellel M., Wathelet M., Machane D., Bensalem R., et al. The relationship between ambient vibration H/V and SH transfer function: some experimental results. *Seismol Res Lett* 2016;87:1112–1119. doi:10.1785/0220160113.
- [21] Foti S., Parolai S., Albarello D., Picozzi M. Application of surface-wave methods for seismic site characterization. *Surv Geophys* 2011;32:777–825. doi:10.1007/s10712-011-9134-2.
- [22] Farrugia D., Paolucci E., D’Amico S., Galea P. Inversion of surface wave data for subsurface shear wave velocity profiles characterized by a thick buried low-velocity layer. *Geophys J Int* 2016;206:1221–1231. doi:10.1093/gji/ggw204.
- [23] Zhao J.X., Zhang J., Asano A., Ohno Y., Oouchi T., Takahashi T., et al. Attenuation relations of strong ground motion in Japan using site classification based on predominant period. *Bull Seismol Soc Am* 2006;96:898–913. doi:10.1785/0120050122.
- [24] Di Alessandro C., Bonilla L.F., Boore D.M., Rovelli A., Scotti O. Predominant-Period site classification for response spectra prediction Equations in Italy. *Bull Seismol Soc Am* 2012;102:680–695. doi:10.1785/0120110084.
- [25] Derras B., Bard P.-Y., Cotton F. VS30, slope, H800 and f0: performance of various site-condition proxies in reducing ground-motion aleatory variability and predicting nonlinear site response. *Earth Planets Space* 2017;69:1–21. doi:10.1186/s40623-017-0718-z.
- [26] Hassani B., Atkinson G.M. Site-effects model for central and Eastern North America based on peak frequency and average shear-wave velocity. *Bull Seismol Soc Am* 2018;108:338–350. doi:10.1785/0120170061.
- [27] Pitilakis K., Riga E., Anastasiadis A., Fotopoulou S., Karafagka S. Towards the revision of EC8: proposal for an alternative site classification scheme and associated intensity dependent spectral amplification factors. *Soil Dynam Earthq Eng* 2019;126:105137. doi:10.1016/j.soildyn.2018.03.030.
- [28] Zhu C., Pilz M., Cotton F. Which is a better proxy, site period or depth to bedrock, in modelling linear site response in addition to the average shear-wave velocity? *Bull Earthq Eng* 2020;18:797–820. doi:10.1007/s10518-019-00738-6.
- [29] Duval A.M., Bard P.Y., Lebrun B., Lacave-Lachet C., Riepl J., Hatzfeld D. n/v technique for site response analysis. Synthesis of data from various surveys. *Boll Geofis Teor Appl* 2001;42:267–280.
- [30] Rodriguez V.H.S., Midorikawa S. Applicability of the H/V spectral ratio of microtremors in assessing site effects on seismic motion. *Earthq Eng Struct Dynam* 2002;31:261–279. doi:10.1002/eqe.108.

- [31] Schleicher L.S., Pratt T.L. Characterizing fundamental resonance peaks on flat-lying sediments using multiple spectral ratio methods: an Example from the Atlantic coastal plain, Eastern United States. *Bull Seismol Soc Am* 2021;111:1824–1848. doi:10.1785/0120210017.
- [32] Zhu C., Cotton F., Pilz M. Detecting site resonant frequency using HVSR: fourier versus response spectrum and the first versus the highest peak frequency. *Bull Seismol Soc Am* 2020;110:427–440. doi:10.1785/0120190186.
- [33] Kawase H., Sanchez-Sesma F.J., Matsushima S. The optimal use of horizontal-to-vertical spectral ratios of earthquake motions for velocity inversions based on diffuse-field theory for plane waves. *Bull Seismol Soc Am* 2011;101:2001. doi:10.1785/0120100263. –14.
- [34] Rong M., Fu L., Wang Z., Li X., Carpenter N.S., Woolery E.W., et al. On the amplitude Discrepancy of HVSR and site amplification from strong-motion observations. *Bull Seismol Soc Am* 2017;107:2873–2884. doi:10.1785/0120170118.
- [35] Rong M., Li H., Yu Y. The difference between horizontal-to-vertical spectra ratio and empirical transfer function as revealed by vertical arrays. *PLoS One* 2019;14:e0210852. doi:10.1371/journal.pone.0210852.
- [36] Bonnefoy-Claudet S., Kohler A., Cornou C., Wathelet M., Bard P.-Y. Effects of Love waves on microtremor H/V ratio. *Bull Seismol Soc Am* 2008;98:288–300. doi:10.1785/0120070063.
- [37] Schnabel P.B., Lysmer J., Seed H.B. SHAKE: a computer program for earthquake response analysis of horizontally layered sites. Report EERC, 72–12; 1972. Berkeley, USA.
- [38] Peruzzi G., Albarello D., Baglione M., D’Intinosante V., Fabbroni P., Pileggi D. Assessing 1D litho-stratigraphical amplification factor for microzoning studies in Italy. *Bull Earthq Eng* 2016;14:373–389. doi:10.1007/s10518-015-9841-z.
- [39] Paolucci E., Tanzini A., Peruzzi G., Albarello D., Tiberi P. Empirical testing of a simplified approach for the estimation of 1D litho-stratigraphical amplification factor. *Bull Earthq Eng* 2020;18:1285–1301. doi:10.1007/s10518-019-00772-4.
- [40] D’Amico M, Felicetta C, Russo E, Sgobba S, Lanzano G, Pacor F, et al. Italian Accelerometric Archive v 3.1 - Istituto Nazionale di Geofisica e Vulcanologia, Dipartimento della Protezione Civile Nazionale. [Http://ItacaMiIngvIt/ItacaNet\\_31/#/Home2020](http://ItacaMiIngvIt/ItacaNet_31/#/Home2020).
- [41] ASTM (American Society for Testing and Materials). Standard practice for classification of soils for engineering purposes (unified soil classification system). 2017. West Conshohocken, PA.
- [42] Amanti M., Muraro C., Roma M., Chiessi V., Puzzilli L.M., Catalano S., et al. Geological and geotechnical models definition for 3rd level seismic microzonation studies in Central Italy. *Bull Earthq Eng* 2020;18:5441–5473. doi:10.1007/s10518-020-00843-x.
- [43] Pieri P., Sabato L., Tropeano M., Albanelli A., Bertini A., Festa V., et al. Plio-Pleistocene stratigraphic and tectonic evolution of the foreland-foredeep-chain system in Southern Italy. In: Guerrieri L., Rischia I., Serva L., editors. Field trip guide book P35, vol. 4. Rome, Italy: APAT – Italian Agency for the Environmental Protection and Technical Services; 2004. p. 1–44.
- [44] Finetti I.R. CROP project: deep seismic exploration of the central Mediterranean and Italy. Elsevier; 2005.
- [45] Toro G.R. Probabilistic models of site velocity profiles for generic and site-specific ground-motion amplification studies 1995;779574. Upton, New York, USA.
- [46] Kaklamanos J., Bradley B.A., Thompson E.M., Baise L.G. Critical parameters affecting bias and variability in site-response analyses using KiK-net Downhole array data. *Bull Seismol Soc Am* 2013;103:1733–1749. doi:10.1785/0120120166.
- [47] Zhu C., Cotton F., Pilz M. Testing the depths to 1.0 and 2.5 km/s velocity isosurfaces in a velocity model for Japan and implications for ground-motion modeling. *Bull Seismol Soc Am*

- [48] EN 1998-1 Eurocode 8. Design of structures for earthquake resistance-part 1: general rules, seismic actions and rules for buildings. Brussels: European Committee for Standardization; 2005.
- [49] Yokota K., Imai T., Konno M. Dynamic deformation characteristics of soils determined by laboratory tests. *OYO Tec Rep* 1981;3:13–37.
- [50] EPRI (Electric Power Research Institute). Guidelines for determining design ground motions. 1993.
- [51] Darendeli M.B. Development of a new family of normalized modulus reduction and material damping curves. PhD thesis. The University of Texas; 2001.
- [52] Rota M., Zuccolo E., Taverna L., Corigliano M., Lai C.G., Penna A. Mesozonation of the Italian territory for the definition of real spectrum-compatible accelerograms. *Bull Earthq Eng* 2012;10:1357–1375. doi:10.1007/s10518-012-9369-4.
- [53] Albarello D., Lunedei E. Structure of an ambient vibration wavefield in the frequency range of engineering interest ([0.5, 20] Hz): insights from numerical modelling. *Near Surf Geophys* 2011;9:543–559. doi:10.3997/1873-0604.2011017.
- [54] Fäh D., Kind F., Giardini D. A theoretical investigation of average  $H/V$  ratios. *Geophys J Int* 2001;145:535–549. doi:10.1046/j.0956-540x.2001.01406.x.
- [55] Herak M. ModelHVSR—a Matlab® tool to model horizontal-to-vertical spectral ratio of ambient noise. *Comput Geosci* 2008;34:1514–1526. doi:10.1016/j.cageo.2007.07.009.
- [56] Lunedei E., Albarello D. Horizontal-to-vertical spectral ratios from a full-wavefield model of ambient vibrations generated by a distribution of spatially correlated surface sources. *Geophys J Int* 2015;201:1142–1155. doi:10.1093/gji/ggv046.
- [57] Lunedei E., Albarello D. Power spectral density function and spatial autocorrelation of the ambient vibration full-wavefield generated by a distribution of spatially correlated surface sources. *Geophys J Int* 2016;204:1817–1837. doi:10.1093/gji/ggv559.
- [58] Sánchez-Sesma F.J., Rodríguez M., Iturrarán-Viveros U., Luzón F., Campillo M., Margerin L., et al. A theory for microtremor  $H/V$  spectral ratio: application for a layered medium. *Geophys J Int* 2011;186:221–225. doi:10.1111/j.1365-246X.2011.05064.x.
- [59] García-Jerez A., Luzón F., Sánchez-Sesma F.J., Lunedei E., Albarello D., Santoyo M.A., et al. Diffuse elastic wavefield within a simple crustal model. Some consequences for low and high frequencies. *J Geophys Res Solid Earth* 2013;118:5577–5595. doi:10.1002/2013JB010107.
- [60] García-Jerez A., Piña-Flores J., Sánchez-Sesma F.J., Luzón F., Perton M. A computer code for forward calculation and inversion of the  $H/V$  spectral ratio under the diffuse field assumption. *Comput Geosci* 2016;97:67–78. doi:10.1016/j.cageo.2016.06.016.
- [61] E. Lunedei P. Malischewsky A review and some new issues on the theory of the  $H/V$  technique for ambient vibrations A. *Ansal Perspectives on European earthquake engineering and seismology 2015* 371 394 10.1007/978-3-319-16964-4\_15 Springer International Publishing
- [62] Brocher T.M. Empirical relations between elastic wavespeeds and density in the Earth's crust. *Bull Seismol Soc Am* 2005;95:2081–2092. doi:10.1785/0120050077.
- [63] SESAME (Site EffectS Assessment using AMbient Excitations). Guidelines for the implementation of the  $H/V$  spectral ratio technique on ambient vibrations measurements, processing and interpretation. Sesame project-Deliverable D23. 12-WP12- 2004.

---

## Highlights

- Simulation and comparison of a huge set of HVSR curves and SH acceleration transfer functions.
  - Comparisons were focused on peak parameter values ( $F_0$ ,  $A_0$ ,  $F_d$  and  $A_d$ ).
  - HVSR peak is a reliable proxy to identify 1D resonance frequency when  $F_0$  and  $F_d$  coincide.
  - HVSR is less effective proxy for  $F_d$  in the frequency range 10–30 Hz.
  - HVSR tends to underestimate in a similar way both  $A_0$  and  $A_d$  values.
- 

## Appendix A Supplementary data

The following are the Supplementary data to this article:

 [Multimedia Component 1](#)

---

### Multimedia component 1

alt-text: Multimedia component 1

 [Multimedia Component 2](#)

---

### Multimedia component 2

alt-text: Multimedia component 2

## Queries and Answers

Q1

**Query:** Correctly acknowledging the primary **funders and grant IDs** of your research is important to ensure compliance with funder policies. Please make sure that funders are mentioned accordingly.

**Answer:** Reviewed

Q2

**Query:** Please confirm that the provided **email** “enricopaolucci83@gmail.com” is the correct address for official communication, else provide an alternate e-mail address to replace the existing one, because private e-mail addresses should not be used in articles as the address for communication.

**Answer:** Reviewed

Q3

**Query:** Please check the article title and amend if necessary.

**Answer:** The article title is correct

Q4

**Query:** Please check whether the **hierarchy of the section headings** are as expected. If changes are needed, please use the comment option to indicate the required changes

**Answer:** Reviewed

Q5

**Query:** Please confirm that **given names and surnames** have been identified correctly and are presented in the desired order and please carefully verify the spelling of all authors' names.

**Answer:** Reviewed

Q6

**Query:** Your article is registered as a regular item and is being processed for inclusion in a regular issue of the journal. If this is NOT correct and your article belongs to a Special Issue/Collection please contact [h.gopu@elsevier.com](mailto:h.gopu@elsevier.com) immediately prior to returning your corrections.

**Answer:** The article does **NOT** belong to a Special Issue/Collection